

## Chapter 3

# Dark Measurement Results

The measurements taken can be neatly divided into dark measurements, where the array and cryostat windows were covered to keep optical radiation from reaching the array, and measurements under illumination, where a controlled radiation source was placed in front of the cryostat window to illuminate the detector. Both types of measurement are of interest for characterizing this array; the dark measurements offer a glimpse into the operating capabilities under very low light conditions and allow the most fundamental and characteristic noise sources to dominate and be studied. In contrast the illuminated measurements are more similar to how this array might be used for science so they provide a more concrete picture of the array's potential performance. I will begin by presenting the dark measurement results and later compare these to the illuminated measurement results.

### 3.1 Temperature dependence

The simplest experiment to carry out is to vary the temperature of the device and record the changes in the resonance. A detector pixel responds to changes in temperature and changes in incident radiation similarly since both processes result in additional Cooper pair-breaking energy in the inductor. Thus we expect to see both the resonant frequency  $f_r$  and the quality factor  $Q_i$  of the resonance varying with temperature, which was observed (Fig. 3.1). Also shown in the figure is the best fit of a theoretical model based on the Mattis-Bardeen theory of superconductivity. The model is derived in Appendix A. To fit  $f_r(T)$ , the superconducting transition temperature  $T_c$  was allowed to vary;  $T_c = 13.7K$  yielded the best fit.  $Q_i^{-1}(T)$  depends both on  $T_c$  and the kinetic inductance fraction  $\alpha$ , defined as the ratio of the kinetic inductance  $L_k$  to the total inductance  $L_k + L_s$ , where  $L_s$  is the temperature-invariant geometric inductance. For this fit we fixed  $T_c$  at the value determined from the fit to  $f_r(T)$  and varied  $\alpha$ .  $\alpha = 0.55$  gave the best fit.

Finally, the inverse quality factor was plotted against fractional frequency shift to yield Fig. 3.1b. The slope of the fit to the left-most points is  $\beta$ , the ratio of the change in frequency to the change in dissipation from the same signal. Our device has  $\beta \sim 35$ , indicating the frequency change is larger.

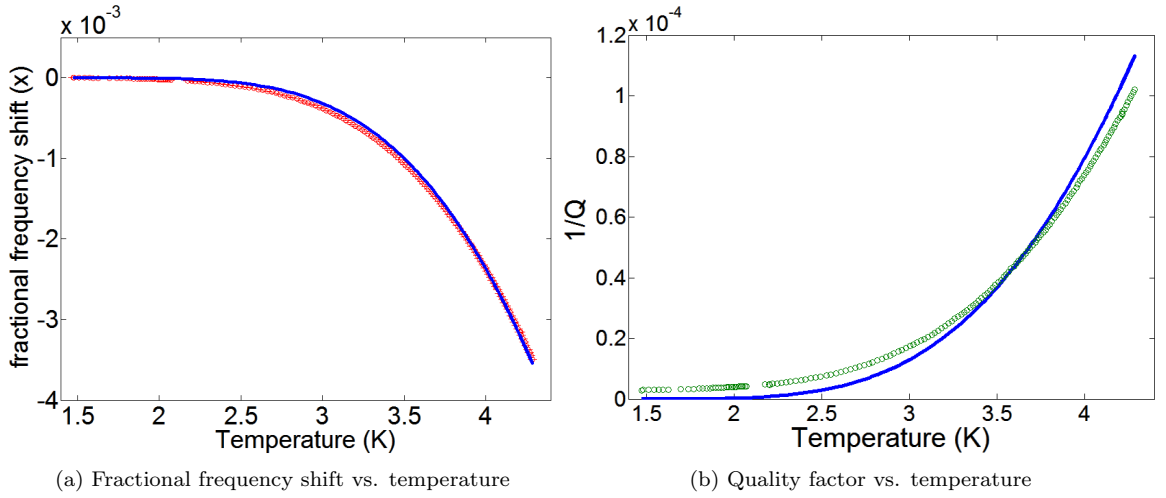


Figure 3.1: (a) Fractional frequency shift  $x$  vs. temperature. The data points are plotted in red, with the fit from Mattis-Bardeen theory (Appendix A) in blue. The fit is a best fit line; the superconducting transition temperature  $T_c$  was allowed to vary to find the curve which best matched the data. The shown curve corresponds to  $T_c = 13.7K$ , which is the value the material was designed to have. (b) Inverse quality factor vs. temperature. The theory predicts that  $Q \rightarrow \infty$  as  $T \rightarrow 0$ . In this and other superconducting microresonator-based devices however,  $Q$  is observed to approach a finite maximum; this is due to other sources of dissipation, including TLS (Section 1.2.5) and radiation into free space [15]. The gap in the data near 2.2 K is the lambda point of liquid helium, where it transitions from superfluid to normal liquid and the associated large change in heat capacity causes a jump in the temperature.

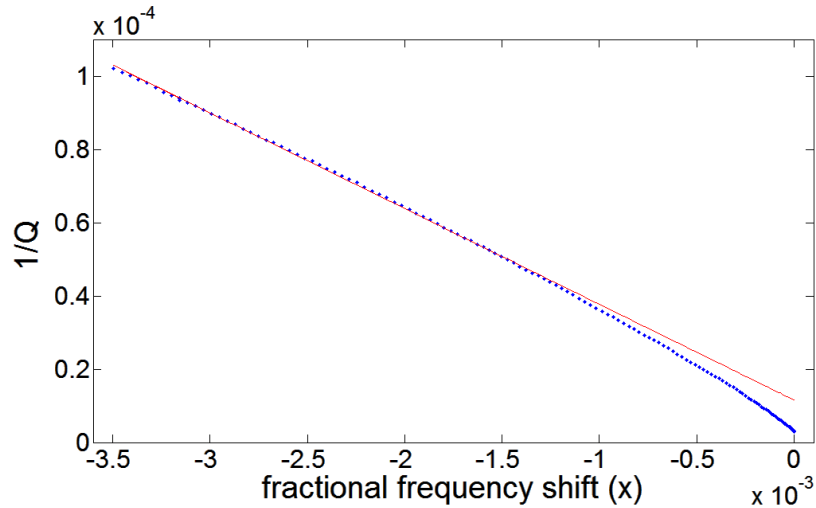


Figure 3.2: Inverse quality factor vs. fractional frequency shift. For the region where Mattis-Bardeen theory is valid, the points map to a line whose slope is  $\beta$ , the ratio of the change in frequency to the change in dissipation from the same signal. Our device has  $\beta \sim 35$ , indicating the frequency change is much larger.

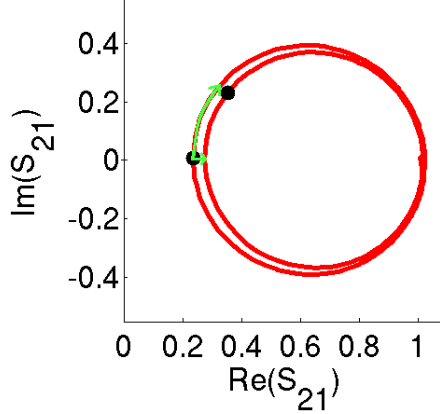


Figure 3.3: To measure a signal change, resonances sampled before and after a change in incident power are compared. The resonant frequency  $f_r$  before the change is at a different position after the change; the fractional frequency shift  $x$  is thus  $(f_{r_{old}} - f_{r_{new}})/f_{r_{new}}$ . The signal change in the dissipation direction is also shown.

## 3.2 Response

With the basic behavior of the resonances understood, the next step was to look toward the measurements necessary to find out the sensitivity of the array. The sensitivity depends both on the magnitude of the response of the resonator to a small change in the incident power and the random fluctuations, or noise, in the resonator properties measured. If the power change results in a response so small that it cannot be distinguished from the random fluctuations, then the detector is not sensitive enough to observe that change. More precisely, the sensitivity for long wavelength detectors is usually given as the noise equivalent power, defined for noise  $S_{xx}$  and response  $R$  as

$$NEP = \frac{\sqrt{S_{xx}}}{R}. \quad (3.1)$$

Thus accurate measurements of both the response and the noise are necessary to estimate the NEP.

Signal changes are measured by comparing a resonance before and after a small change in the incident power. Because both reactive and dissipative changes occur, either or both of these changes may be measured independently to infer the change in incident power. Changes in the resonant frequency (reactive) are along the resonance loop and dissipation changes are perpendicular to it (Fig. 3.3). The response is significantly larger in the frequency direction as a consequence of superconductivity theory. This makes the frequency direction less susceptible to electronic noise; for this reason, we focus on the response and noise measurements in the frequency direction only. The signal change produces a response in the form of a fractional frequency shift  $x$ , given by Eq. (2.2). Note that in a system where this detector is used for science applications, both directions may be used.

The response was measured with and without light allowed into the cryostat. In the former case,

the mechanism is straightforward; a change in the incident power causes changes in the resonance as described above. In the latter case, small temperature changes serve as the effective signal. These may be converted to equivalent changes in incident power by  $G$ , the thermal conductance of the bolometer island legs:

$$G\Delta T = \Delta P.$$

The response under dark conditions is thus

$$R = \frac{\Delta x}{G\Delta T}.$$

### 3.2.1 Thermal conductance calculation

$x/\Delta T$ , the response to temperature changes, is readily calculated as the derivative of the curve in Fig. 3.1a. The other necessary quantity is the thermal conductance  $G$  of the bolometer island legs. It is known empirically that  $G$  exhibits a roughly  $T^3$  dependence [1]. From the phonon NEP expression given in Section 1.1.1 and Eq. (3.1), we can solve for  $G$ :

$$G = \frac{4k_B T^2 (\Delta x / \Delta T)^2}{S_{xx}^{\text{phonon}}}$$

where  $S_{xx}^{\text{phonon}}$  is the phonon contribution to the total noise  $S_{xx}$ . Measurements of the phonon noise (see Section 3.3.3 below) fit to a  $T^3$  power law yield, in nW/K,

$$G \approx 0.3T^3.$$

### 3.2.2 Results

The response is shown as a function of temperature in Fig. 3.4. Importantly, there is well over an order of magnitude difference between the response at 1.5 K and at 4 K, suggesting that the lowest temperatures will not yield the optimal sensitivity.

## 3.3 Noise

### 3.3.1 Data collection and processing

The noise is first measured by sampling a resonance and then outputting a single tone from the signal generator at the resonant frequency. Sampling at this position for several seconds yields a spread of data points representing the noise (Fig. 3.5). Like the response, the noise may be measured in either the frequency direction or the dissipation direction, or both; we chose the frequency direction

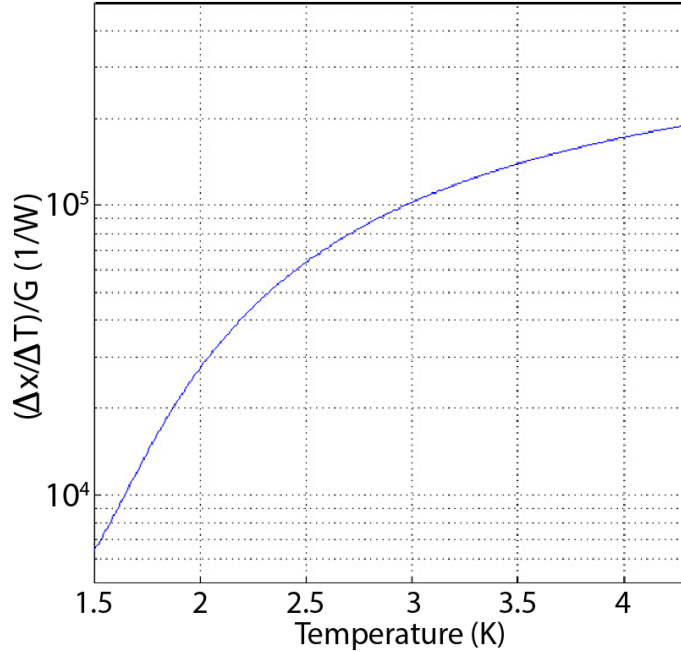


Figure 3.4: Calculated response from  $G = 0.3T^3$  nW/K.

for reasons stated above (Sec. 3.2). From the initial scan of the resonance, a mapping between the generator frequencies and the points on the resonance loop is made, and the fractional frequency shift  $x$  for each point is calculated (Eq. (2.2)).

Next, the power spectral density of the time stream of data is computed. The power spectral density quantifies the power carried by each frequency component of a stochastic process (in this case, the noise data stream) and is typically given in Watts/Hz. This is normalized by dividing by the total power in the signal to yield the fractional frequency noise  $S_{xx}$  in  $(\text{Hz})^{-1}$ .

### 3.3.2 Noise sources

A typical set of noise plots for one pixel are shown in Figure 3.6. Several distinct processes contribute to the observed noise. Phonon noise from quantized fluctuations in thermal energy in the bolometer island legs (section 1.1.1) introduce noise up to about 150 Hz, where the noise is low-pass filtered by the thermal time constant  $\tau$  (see sections 1.1 and 4.2). At lower frequencies, electronics and thermal instability associated with pumping on a liquid helium bath increase the noise. At the highest frequencies, two different noise sources dominate at different temperatures. At low  $T$ , two level system noise (see section 1.2.5) dominates. It is low-pass filtered by the resonator ring-down time constant (see Appendix B). At high  $T$  the resonator  $Q$  decreases significantly. This leads to a relatively increased electronic contribution at high noise frequencies ( $> \sim 1\text{kHz}$ ). It, along with all the other noise sources, is rolled off by an anti-aliasing 100 kHz low-pass filter. Finally, the sharp noise spikes originate from the electronics.

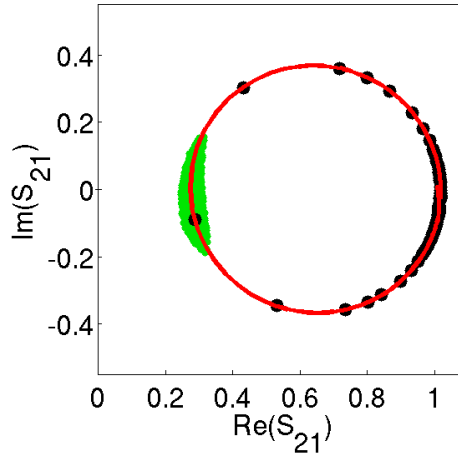


Figure 3.5: Noise at resonance. Each data point in the green spread is mapped to a frequency using the fit to a frequency scan over the resonance (black points).

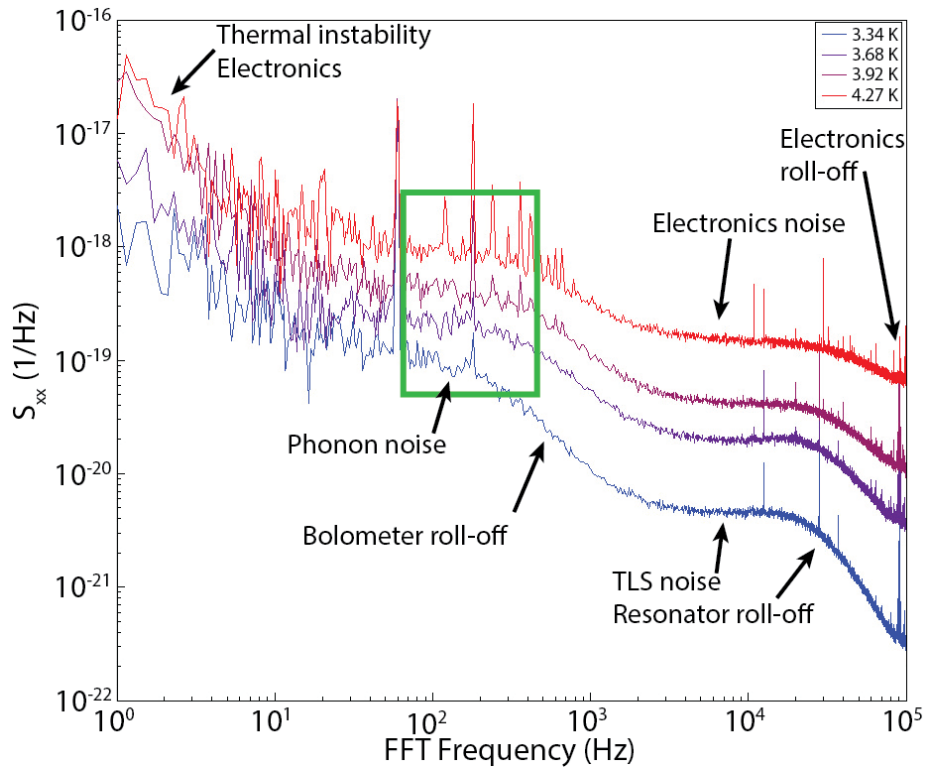


Figure 3.6: Example fractional frequency noise plots at various temperatures. The green box indicates the frequencies of interest for the NEP calculation; higher frequencies will not be used for science applications and non-detector-based noise takes over at lower frequencies.

### 3.3.3 Dark noise results

In practice, signals varying with frequencies above the bolometer roll-off cannot be observed with this detector because the averaging effect of the bolometer time constant will reduce the signal. Thus the frequencies of interest for operation are  $\sim 150$  Hz and below. Extraneous noise from thermal drift and excess noise exhibited by our cryogenic amplifier dominate at very low frequencies. In the future, these can be greatly reduced with a new amplifier and a thermally controlled sample stage. For this measurement however, the value of  $S_{xx}$  used to calculate the NEP is an average of the data points within the green box in Fig. 3.6, excluding the electronic noise spikes. This average noise is plotted vs. temperature in Fig. 3.7. A clear minimum is visible at  $\sim 2.5$  K; to either side, the two most important noise sources dominate. At high temperatures, the phonon noise dominates; it is given by

$$S_{xx}^{\text{phonon}} = \frac{4k_B T^2 (\Delta x / \Delta T)^2}{G}.$$

The plotted phonon noise curve is a best fit of this equation to the data, with  $G$  as a variable parameter.  $G = 0.3T^3$  nW/K yields the best fit; thus this was the dependence chosen for the response calculation (section 3.2).

At the low temperature end, the TLS noise dominates due to its  $T^{-2}$  dependence. The exact proportionality constant for this dependence was also chosen for its fit to the data; thus

$$S_{xx}^{\text{TLS}} = \frac{3 * 10^{-19} \text{ K}^2/\text{Hz}}{T^2}.$$

Added together, these two sources predict the temperature dependence of the noise nicely. The next step is to combine the noise data with the response data to get the NEP. This is done at the end of chapter 4 together with the NEP under illuminated conditions.

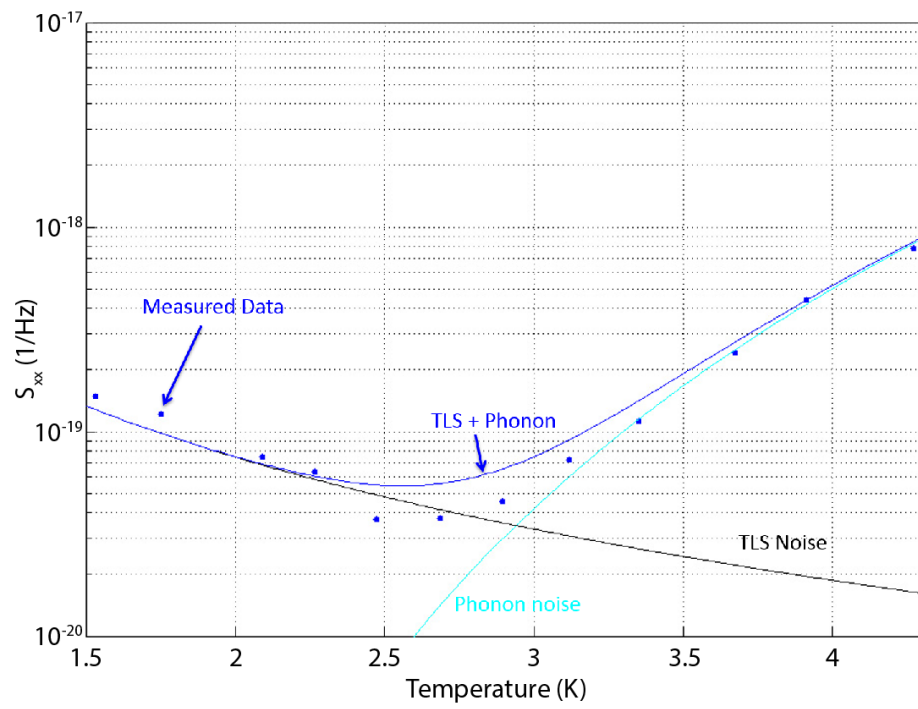


Figure 3.7: Noise under dark conditions. Phonon noise dominates at high temperatures, while TLS noise dominates at low temperatures.